COMMUNICATION

Large scale ZrS₂ atomically thin layers†

Xiaoting Wang, Le Huang, Xiang-Wei Jiang, Yan Li, Zhongming Wei* and Jingbo Li*

We present the scalable synthesis of large scale (up to 30 μm in lateral size), single-crystalline, atomically thin hexagonal ZrS₂ nanoflakes *via* an optimized chemical vapor deposition (CVD) method on traditional substrates (silica, sapphire). The Vienna *ab initio* simulation package (VASP) was employed to calculate the adhesion energy and provided an exact theoretical account for the substrate and temperature dependent growth process of ZrS₂ nanoflakes. Photodetectors based on ZrS₂ nanoflakes were fabricated and displayed a remarkable photoconductivity under visible light. Field-effect transistors based on ZrS₂ monolayers exhibited obvious n-type transport characteristics with relatively high mobility.

The rise of controlled processing and versatile properties in graphene in the past decade has led to broad interest in other two-dimensional (2D) systems. In the family of 2D materials, transition-metal dichalcogenide (TMD) materials attracted tremendous attention due to their distinctive geometries, peculiar physical properties and various applications in nanodevices.[1–7] 2D TMDs of different types (such as insulating h-BN, semiconducting MoS₂, WS₂, WSe₂, *etc.*) have been synthesized on multifarious substrates, *via* various growth methods and using a variety of reactants as precursors.[8–18] Among those methods, use of chloride and sulfur as precursors has advantages such as requiring low-melting evaporable reactants, difform disulphide and achieving few additional products. For example, MoS₂ and WS₂ fullerene-like nanostructures and nanoflowers have been obtained by the reaction of chlorides (MoCl₅/WCl₆) with sulfur under controlled conditions.[19] 1–3 μm hexagonal NbS₂ nanosheets have been reported using the NbCl₅ powder as a precursor, instead of the high-melting nickel or niobium oxide powder.[20]

As a typical semiconducting group among TMDs, ZrX₂ (X = S, Se and Te) compounds belong to the space group $P\bar{3}m1$, which has a hexagonal close-packed sulfide lattice with metal atoms in alternate layers of the octahedral holes.[21–23] ZrS₂ materials combined with the small effective mass display a large upper limit of acoustic limited mobility (1200 cm² V⁻¹ s⁻¹), even three times larger than that of widely studied MoS₂ (340 cm² V⁻¹ s⁻¹).[24] Due to a bandgap of 1.4 eV, the absorption peaks of ZrS₂ materials should be located within the range from 400 to 760 nm, the visible-light region and the origin of most solar energy.[25,26] Various nanostructured ZrS₂ materials such as nanoflakes, nanobelts and nanotubes have been prepared based on the hexagonal structure.[25,27–29] But large scale ZrS₂ structures on the order of micrometers were rarely employed. Such a size limitation restricts their exploration in 2D nanodevices.

It seems that the substrate can be one decisive factor for the nucleation rate during the growth of ZrS₂ nanostructures.[30,31] Recently, Liming Xie and co-workers made a great effort to achieve a 2D hexagonal ZrS₂ monolayer and few layers with a domain size of about 1–3 μm, where hexagonal boron nitride (hBN) was used as the deposition template for the growth.[28] Hexagon-shaped ZrS₂ has revealed a restricted crystallographic orientation that is strictly related to the underlying hBN. The preparation of large scale ZrS₂ sheets on traditional substrates which are suitable for the general optoelectronic device fabrication remains a challenge. Herein, we report the growth of thin hexagonal ZrS₂ nanoflakes by direct CVD on traditional insulators (silica, sapphire) including bare Si/SiO₂ substrates, with large size from 7 to 30 μm. The results here showed that the substrates exert a great influence on factors for the growth such as growth conditions, size and shape. The Vienna *ab initio* simulation package (VASP) was employed to calculate the adhesion energy and provided an exact theoretical account for large-size and semi-hexagonal ZrS₂ nanoflakes as-grown on silica or BN. Photodetectors based on ZrS₂ nanosheets were fabricated on Si/SiO₂ wafers and displayed a remarkable photoconductivity under the visible light source.[26]

The method used here was an optimized CVD process with controlled gas flow. Two traditional insulators (including silica and sapphire) functioned as substrates for the growth of ZrS₂.

State Key Laboratory of Superlattices and Microstructures, Institute of Semiconductors, Chinese Academy of Sciences, P.O. Box 912, Beijing 100083, China. E-mail: zmwei@semi.ac.cn, jbli@semi.ac.cn

This journal is © The Royal Society of Chemistry 2016
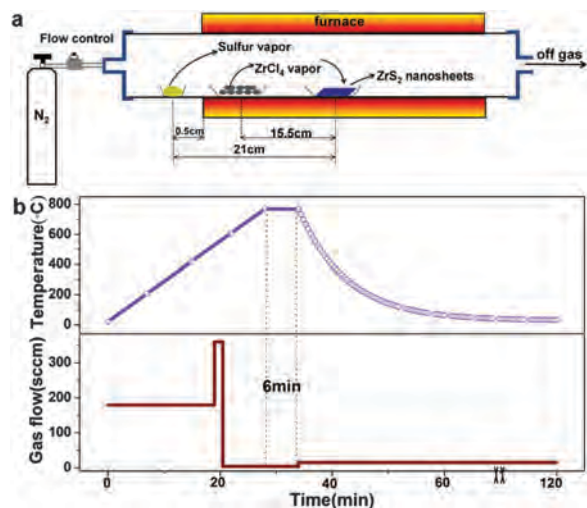
J. Mater. Chem. C, 2016, 4, 3143–3148 | 3143

Fig. 1 (a) Configuration used in our experiments for the growth of ZrS_2 nanosheets; (b) monitored temperatures and nitrogen gas flow of the central alumina boat with time.

Fig. 2 (a) In-plane atomic arrangement structure of ZrS_2, with violet and metallic grey microspheres representing Zr and S; (b) the Raman mapping at the Raman mode of 333 cm^{-1} and microscope image (inset) of ZrS_2; (c) the Raman scattering spectra A, C and D of bulk, six-layer, three-layer hexagonal nanoflakes on silica and spectra B of bulk nanoflakes on sapphire. All of the scale bars are 10 μm.

High quality and large scale 2D ZrS_2 nanoflakes were achieved on both substrates. Atomically thin monolayers and multilayers were observed. Fig. 1a shows a schematic diagram of the single-furnace CVD apparatus for the synthesis of ZrS_2 nanosheets on silica or sapphire. The central growth temperature and the nitrogen (N_2) gas flow were in accordance with those in Fig. 1b. A burst of N_2 flow at 500–540 °C occurred to drive away premature excess $ZrCl_4$ vapor and prevent the over- or undersupply of chloride and sulfur. Apart from the reported 2D BN crystalline substrate, the valid records of such amorphous insulators here efficiently extend the range of substrates and also further indicated substrate-dependent growth of ZrS_2 nanoflakes.

ZrS_2 has a similar layered structure to the commonly reported TMD of MoS_2. Differently, the most stable crystal structure of ZrS_2 crystallizes in the tetragonal (T) phase (as displayed in Fig. 2a) in comparison with the hexagonal (H) phase in MoS_2.[32] And its S–Zr–S sandwich layers are stacked with a periodicity of one layer and a global D_{3d} space-group symmetry. The structural simplicity of ZrS_2—the unit cell only spans one layer—is reflected in the Raman spectra, which theoretically consists of just two modes, E_g and A_{1g}.[33] Its A_{2u} resonant modes can also be observed. As shown in spectra A, B and C of Fig. 2c, the E_g mode, the A_{1g} mode and the A_{2u} mode of ZrS_2 samples grown on Si/SiO_2 and sapphire substrates are located at 247 cm^{-1}, 333 cm^{-1}, and 313 cm^{-1}, respectively. But it is apparent to observe that the three-layer sample (spectrum D; dotted line) has almost no Raman signal, only the SiO_2 signal is detected, which may probably be ascribed to the weak Raman peak intensity of samples with 3L or fewer layers in itself. After all, the Raman peak of six-layer ZrS_2 is rather weakened in comparison with that of bulk ZrS_2 in Fig. 2c. Meanwhile, the mapping image of the A_{1g} mode for about 15 nm-ZrS_2 nanoflakes was acquired (Fig. 2b), clearly indicating a hexagonal shape, and confirming the uniformity and integrity of ZrS_2 growth on silica.
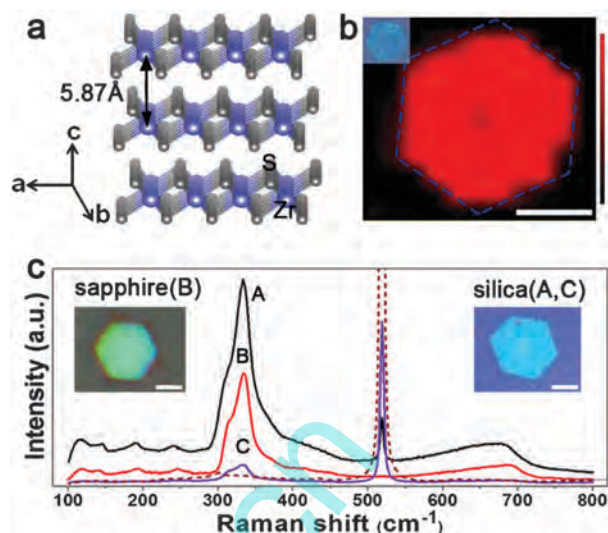
The synthetic nanosheets also exhibit excellent crystalline quality. Fig. 3b and c shows the high resolution TEM (HRTEM) image of the obtained ZrS_2 nanosheets and the corresponding selected-area electron diffraction (SAED) pattern. An interplanar spacing of 3.65 Å (along the red line revealed in Fig. 3b) corresponds to the (100) (Point A) or (010) (Point B) plane along the [001] crystal zone axis (Point O as the center diffraction spot). The reflections have been indexed to the hexagonal structure of ZrS_2 with lattice constants: a = 3.65 Å, c = 5.81 Å. The HRTEM and SAED results indicate a single-crystal hexagonally symmetrical structure of the ZrS_2 nanosheets. The analysis of the corresponding energy-dispersive X-ray spectrum (TEM-EDX)
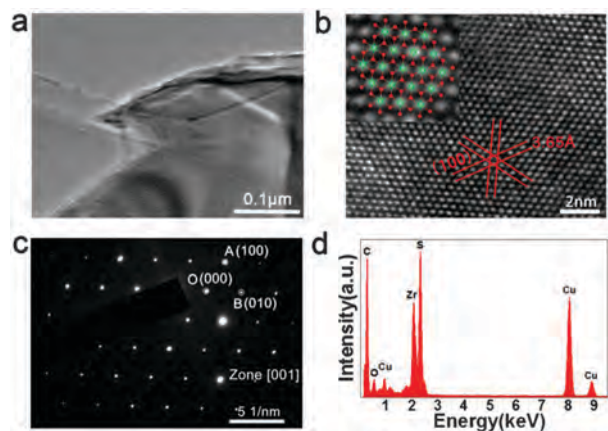

Fig. 3 (a) Low-magnification TEM image of hexagonal ZrS_2 nanosheets supported on a holey carbon grid; (b) HRTEM image of ZrS_2 and the corresponding atomic arrangement structure of ZrS_2 (inset); (c) corresponding SAED pattern of the nanosheet in (a); (d) corresponding TEM-EDX profile of the sample.

(Fig. 3d) demonstrates that the nanosheet consists of Zr and S elements (the exhibited C, Cu and O peaks arise from the carbon film, copper net and adhesive from the sample desk, respectively). And it can be determined from the EDX spectrum that the atomic composition was $ZrS_{1:1.7}$, in approximate agreement with the ratio of ZrS_2. SEM-EDX is further employed to confirm the composition of the nanosheets and the result is close to TEM-EDX (see the ESI,† Fig. S1).

In addition to the substrates, the reaction temperature is another critical factor in the process of synthesizing ZrS_2 ultrathin films. When the reaction temperature was set at 730 °C for 6 minutes, the entire SiO_2 substrate was covered with only white $ZrCl_4$ particles. As the temperature was increased to 760 °C, hexagonal ZrS_2 slices with a small defect point were found. Large-size monolayer, bilayer, trilayer and multilayer hexagonal ZrS_2 emerged at around 770 °C (SEM images in Fig. 4a, the corresponding local optical images in Fig. 4b, and the atomic force microscopy (AFM) images presented in Fig. 4e), the optimized deposition temperature, whereas only little hollow thick hexagonal ZrS_2 were grown on the substrate at 830 °C. Thus it can be inferred that $ZrCl_4$ vapor ought to break into Cl_2 in the transport process and intermediate products of $ZrCl_xS_y$ could not exist at a temperature of 760 °C or greater, as observed in the reaction between sulfur and molybdenum chlorides ($MoCl_5$). Thus, pure ZrS_2 products can be achieved at a temperature higher than 760 °C. The reaction between the chlorides and S in our experiment was formulated as given in eqn (1):

$$ZrCl_4(g) + 6S(g) \rightarrow ZrS_2(s) + 2Cl_2S_2(g) \qquad (1)$$

With the substrate temperature set at 770 °C and the reaction time at 6 minutes, a series of controlled experiments were conducted next at the sulfur vapor concentration, which largely depends upon the flux of the carrier gas. For small amounts of sulfur, the six vertices of the hexagon were connected with ribbon-shaped strips, and some unreacted particles were observed on the substrate due to the inadequate sulfurization. Moderate amounts of sulfur contributed to the forward reaction (eqn (1)) and smooth, 30 μm large hexagonal ZrS_2 atomically thin flakes were obtained. Upon further increasing the N_2 flow rate, the as-grown ZrS_2 nanoflakes displayed a high density, flat surface and semi-hexagonal shape (SEM images in Fig. 4c and the corresponding local optical images in Fig. 4d). Specific images are presented in the ESI,† Fig. S2.

By adjusting the substrate temperature and the flux of the carrier gas, ZrS_2 nanosheets of various micro-patterns and sizes could be acquired. The growth mechanism for the abovementioned nanosheets is discussed by means of the dynamics behavior. $ZrCl_4$ and sulfur powders were sublimated to vapor and were transported onto the receiving substrates by a driven quantitative flow of carrier gas, a critical factor for the diffusion of precursors and deposition of ZrS_2 molecules. Afterwards, reaction in eqn (1) was carried out between absorbed molecules at the substrate temperature. ZrS_2 molecules as the resultant got across the surface potential barrier to the growth sites and were incorporated into the crystalline lattices, which was primarily impacted by the surface migration, or substrate temperature.[34]

Based on the in-plane lattice parameters of ZrS_2 materials ($a_f = 3.65$ Å) and the SiO_2 substrate ($a_s = 4.914$ Å), the misfit of ZrS_2/SiO_2 structures is estimated to be around 34%.[35] The lattice mismatch at the interfaces induces the strain energy for ZrS_2 thin nanoflakes, which forces the layer-by-layer growth (Fig. 5a) (the Frank–Van der Merwe mode) to change into cluster growth (Fig. 5b) due to the lattice relaxation.[36,37] Thus, the optimum temperature for the growth of ZrS_2 nanoflakes
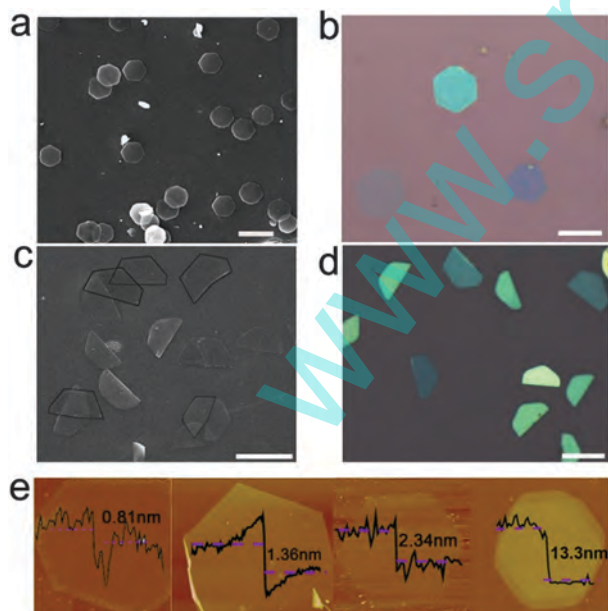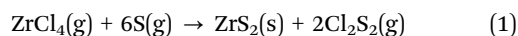

Fig. 4 (a) SEM images of high-density thin-layer hexagonal ZrS_2 crystals; (b) corresponding local optical microscope images of ZrS_2 samples in (a). (c) SEM images of high-density semi-hexagonal ZrS_2 crystals; (d) corresponding local optical microscope images of ZrS_2 samples in (c); (e) typical AFM images of monolayer, bilayer, trilayer and few layer hexagonal ZrS_2 crystals; all of the scale bars are 20 μm.

Fig. 5 (a) The layer-by-layer growth model at 770 °C on silica; (b) the cluster growth model of the ZrS_2 nanosheet at 830 °C on silica; the theoretical calculation model (c) for ZrS_2/BN, (d) for ZrS_2/SiO_2, with the top layer representing ZrS_2 and the below four layers representing the substrates.

This journal is © The Royal Society of Chemistry 2016

J. Mater. Chem. C, 2016, 4, 3143–3148 | 3145

should meet the following demands: enough high to epitaxial growth (greater than 760 °C), and not over-high to prevent molecules with high frequency vibration from cluster growth (less than 830 °C). Of course, in the case of high gas flow, excessive reactant sources have difficulty in migrating from the surface to the hexagonal edge within the limited time, which is probably the main reason for the semi-hexagon shape.

Analyzing the surface properties of substrates and the sample/substrate interfacial compatibility is essential to understand the initial nucleation and growth of nanostructures. In order to further investigate the substrate dependent process of ZrS_2, the adsorption energies of ZrS_2/SiO_2, and ZrS_2/BN in contrast, were theoretically calculated via VASP. Basic units used for calculation are, respectively, composed of 2×3 ZrS_2/BN primitive cells and 3×2 $ZrS_2 \times SiO_2$ primitive cells. Their theoretical models are displayed in Fig. 5c and d. The computational results reveal 0.421 and 0.696 eV on the SiO_2 and BN substrates separately for each ZrS_2 primitive cell, using the formula $\Delta E = E_{total} - E_{ZrS_2} - E_{substrate}$ (ΔE is the adsorption energy between the surface of ZrS_2 and the substrate).[38–40] As a result, ZrS_2 as-grown on silica exhibited weaker adhesion and greater free degree than that on BN with a hexagonal crystal structure. The low absorbed energy of silica enhances the surface diffusion of Zr and S adatoms on the substrate, weakening the confined growth of the substrate and allowing the lateral growth of ZrS_2 nanosheet nuclei. Thus hexagon-shaped ZrS_2 on the BN presented restricted growth with a size of 1–3 μm, the same as other 2D materials grown on the BN such as WS_2 and Mn-doped MoS_2.[8,30] In contrast, 7–30 μm hexagon-shaped ZrS_2 has grown on silica, but too high temperature or excessive sulfur leads to the growth of hollow and semi-hexagonal ZrS_2 nanosheets due to less dependence on the substrate. The VASP provided a fundamental theoretical account for large-size and semi-hexagonal ZrS_2 nanoflakes as-grown on silica.

Photodetectors based on the obtained ZrS_2 nanosheets were fabricated and a series of monochromatic lights were directed vertically onto devices to measure their photoresponse behavior, the schematic diagram and the optical image are presented in Fig. 6a and b. Monolayer ZrS_2 with a thickness of 0.725 nm was used, as shown in the inset of Fig. 6b. The electronic band structures of 2D ZrS_2 nanoflakes were calculated using the VASP.[41] The generalized gradient approximation (GGA) of the Perdew, Burke and Ernzerhof (PBE) functional is employed for electron exchange and correlation.[42] The theoretical calculation displays (Fig. 6c) bandgaps of ZrS_2 with monolayer, three-layer and bulk samples, around 1.4 eV (885 nm), which are consistent with those of 1D ZrS_2 nanobelts.[25,43] Thus light with excitation energy higher than the band gap will produce electron–hole pairs and increase the photocurrent gradually. Fig. 6d depicts the typical I–V curves of ZrS_2 both in the dark and under 1.2 mW cm^{-2} laser illumination. It can be observed that the device showed wavelength selectivity and was most sensitive to violet light (450 nm), moderately sensitive to green light (540 nm), and worst sensitive to red light (630 nm). Besides, the photocurrent indicates a distinctly absolute increment by nearly 2 times (Fig. 6e) under a violet laser. As the optical wavelength decreases, the photon energy increases and can induce
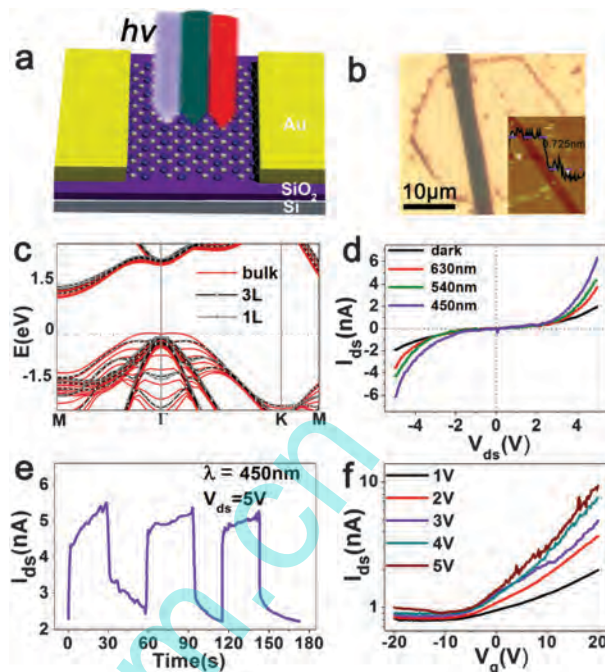

Fig. 6 (a) Illustration of a 2D ZrS_2-based device illuminated with various lights; (b) optical image of the ZrS_2 device with patterned electrodes. The inset shows the AFM image of the ZrS_2 device; (c) energy band plots of monolayer, three-layer and bulk ZrS_2 samples; (d) I_{ds}–V_{ds} curves of the ZrS_2-based device in the dark (black curve) and with visible light illumination (450 nm, 540 nm, 630 nm; power density: 1.2 mW cm^{-2}); (e) I_{ds}–T curve with the violet light switched on/off at V_{ds} = 5 V; (f) transfer characteristics of the devices in the dark at various drain-source voltages in the log coordinate.

more electrons to jump from the valence band to the conduction band. By irradiating light of 450 nm at 1.2 mW cm^{-2}, the photo responsivity value of the present ZrS_2 becomes 2.86 A W^{-1}. The performance parameters are better or in parallel to those of other extant photodetectors such as three-layer MoS_2 or four-layer GaSe, 0.57 and 2.8 A W^{-1} separately.[44,45] The devices showed excellent stability and fast response. As the irradiation source is manually turned on/off, the output current I_{ds} can regularly alter in high or low states rapidly. Field-effect transistors (FETs) based on ZrS_2 monolayers exhibited obvious n-type transport characteristics with an estimated mobility of 0.1–0.8 cm V^{-1} s^{-1} (Fig. 6f), consistent with those of ZrS_2 as-grown on BN.[28]

In conclusion, we have successfully synthesized thin hexagonal ZrS_2 nanoflakes on a bare Si/SiO$_2$ substrate using $ZrCl_4$ and S sources, with the size from 7 to 30 micrometers via an optimized CVD process. It is found that the morphology and size of the nanosheets vary with the nitrogen gas flow and temperature. The multiple structural characterizations display that the substrate dependent synthesized ZrS_2 monolayers and few layers have high crystallinity and a distinct crystal orientation. The growth mechanism of the abovementioned nanosheets is discussed by means of the dynamics behavior to illustrate the phenomenon. The VASP was employed to calculate the adhesion energy and provided an exact theoretical account for large-size and semi-hexagonal ZrS_2 nanoflakes as-grown on silica in contrast to the BN substrate.

3146 | J. Mater. Chem. C, 2016, **4**, 3143–3148

This journal is © The Royal Society of Chemistry 2016

Phototransistors based on ZrS_2 nanosheets on the SiO_2/Si substrate displayed a remarkable photoconductivity under the visible light source. This work provides a controllable method for synthesizing large-scale atomically thin 2D systems directly on the traditional substrates, which can open up new vistas of research for the 2D material based functional (opto)electronics.

Experimental section

Growth of ZrS_2 nanoflakes

ZrS_2 nanoflakes were synthesized using a CVD reactor composed of a horizontal quartz tube and a single-zone tube furnace. As illustrated in Fig. 1a, clean Si/SiO_2 (or sapphire) substrates in a ceramic boat were placed face-up at the center of a tube furnace. And the other two ceramic boats loaded with 0.03 g $ZrCl_4$ and sulfur (0.5–1 g) precursors were placed at the first and the middle upstream zones, respectively. Too much S powder was employed to create an atmosphere in which the chlorides could be reacted completely with ZrS_2. Prior to growth, the quartz tube was flushed with high-purity nitrogen (99.9999%) for 20 min to remove the air residue. Then the temperature in the center of the furnace was increased up to 770/830 °C at a rate of 26 °C min^{-1}. The growth of ZrS_2 was maintained for 6 min, followed by the rapid extraction of the substrate from the heating zone. During the reaction, the temperature of the sulfur zone was slightly above 113 °C (melting point of S), and that of the $ZrCl_4$ zone was adjusted around 400 °C, above the melting point of the $ZrCl_4$ source. The N_2 gas flow was in accordance with that in Fig. 6b. A burst of N_2 flow at 500–540 °C occurred to drive away premature excess $ZrCl_4$ vapor. Afterwards, the furnace was cooled to room temperature under N_2 gas flow.

Characterization of ZrS_2 nanoflakes and devices

The Raman measurements were performed on a confocal laser Raman spectrometer (Renishaw Model inVia-Reflex) at a He–Ne laser (532 nm) excitation. The sizes and morphologies of samples were further characterized using a Hitachi S4500 field-emission scanning electron microscope. The thickness values were measured by AFM (Benyuan Nano-Instruments Ldt. Model CSPM 5500A) using the tapping mode. The phase composition and crystallographic structure were acquired using a JEM-2100F high-resolution transmission electron microscope equipped with an energy dispersive X-ray spectroscope. FET characterization was carried out using Agilent B2902 at room temperature. The optoelectronic properties were obtained using the same electrical measurement system combined with several laser sources (450 nm, 540 nm, 630 nm).

Computational method

The calculations were conducted using the projector augmented wave (PAW) method with the generalized gradient approximation of the Perdew–Burke–Ernzerhof (GGA-PBE) exchange–correlation functional in the VASP. The energy cut off for plane-wave expansion was set at 450 eV. A vacuum layer thickness of 15 Å was employed to prevent the correlation between adjacent layers. Brillouin zone (BZ) sampling was processed with Monkhorst Pack

(MP) special k point meshes and a k-point grid of $5 \times 5 \times 1$ was chosen for the calculations. All the structures were fully relaxed using the conjugated gradient method until the Hellmann–Feynman force on each atom was less than 0.1 eV Å^{-1}.

Acknowledgements

References

1 C. Dean, A. F. Young, L. Wang, I. Meric, G. H. Lee, K. Watanabe, T. Taniguchi, K. Shepard, P. Kim and J. Hone, *Solid State Commun.*, 2012, **152**, 1275–1282.

2 C. H. Lee, G. H. Lee, A. M. van der Zande, W. Chen, Y. Li, M. Han, X. Cui, G. Arefe, C. Nuckolls, T. F. Heinz, J. Guo, J. Hone and P. Kim, *Nat. Nanotechnol.*, 2014, **9**, 676–681.

3 Y. J. Zhang, H. L. Dong, Q. X. Tang, S. Ferdous, F. Liu, S. C. B. Mannsfeld, W. P. Hu and A. L. Briseno, *J. Am. Chem. Soc.*, 2010, **132**, 11580–11584.

4 X. F. Li, M. W. Lin, A. A. Puretzky, J. C. Idrobo, C. Ma, M. F. Chi, M. Yoon, C. M. Rouleau, I. I. Kravchenko, D. B. Geohegan and K. Xiao, *Sci. Rep.*, 2014, **4**, 5497.

5 L. M. Xie, *Nanoscale*, 2015, **7**, 18392–18401.

6 Q. F. Gong, L. Cheng, C. H. Liu, M. Zhang, Q. L. Feng, H. L. Ye, M. Zeng, L. M. Xie, Z. Liu and Y. G. Li, *ACS Catal.*, 2015, **5**, 2213–2219.

7 Y. Cui, R. Xin, Z. H. Yu, Y. M. Pan, Z. Y. Ong, X. X. Wei, J. Z. Wang, H. Y. Nan, Z. H. Ni, Y. Wu, T. S. Chen, Y. Shi, B. G. Wang, G. Zhang, Y. W. Zhang and X. R. Wang, *Adv. Mater.*, 2015, **27**, 5230–5234.

8 M. Okada, T. Sawazaki, K. Watanabe, T. Taniguch, H. Hibino, H. Shinohara and R. Kitaura, *ACS Nano*, 2014, **8**, 8273–8277.

9 S. S. Gronborg, S. Ulstrup, M. Bianchi, M. Dendzik, C. E. Sanders, J. V. Lauritsen, P. Hofmann and J. A. Miwa, *Langmuir*, 2015, **31**, 9700–9706.

10 S. L. Zhao, H. Wang, Y. Zhou, L. Liao, Y. Jiang, X. Yang, G. C. Chen, M. Lin, Y. Wang, H. L. Peng and Z. F. Liu, *Nano Res.*, 2015, **8**, 288–295.

11 H. L. Zhou, C. Wang, J. C. Shaw, R. Cheng, Y. Chen, X. Q. Huang, Y. Liu, N. O. Weiss, Z. Y. Lin, Y. Huang and X. F. Duan, *Nano Lett.*, 2015, **15**, 709–713.

12 J. H. Ahn, M. J. Lee, H. Heo, J. H. Sung, K. Kim, H. Hwang and M. H. Jo, *Nano Lett.*, 2015, **15**, 3703–3708.

13 J. P. Shi, D. L. Ma, G. F. Han, Y. Zhang, Q. Q. Ji, T. Gao, J. Y. Sun, X. J. Song, C. Li, Y. S. Zhang, X. Y. Lang, Y. F. Zhang and Z. F. Liu, *ACS Nano*, 2014, **8**, 10196–10204.

14 Y. Y. Li, Z. M. Qi, M. Liu, Y. Y. Wang, X. R. Cheng, G. B. Zhang and L. S. Sheng, *Nanoscale*, 2014, **6**, 15248–15254.

This journal is © The Royal Society of Chemistry 2016

J. Mater. Chem. C, 2016, **4**, 3143–3148 | 3147

15 D. J. Xue, J. H. Tan, J. S. Hu, W. P. Hu, Y. G. Guo and L. J. Wan, *Adv. Mater.*, 2012, **24**, 4528–4533.

16 S. R. Tamalampudi, Y. Y. Lu, R. U. Kumar, R. Sankar, C. D. Liao, K. B. Moorthy, C. H. Cheng, F. C. Chou and Y. T. Chen, *Nano Lett.*, 2014, **14**, 2800–2806.

17 Q. L. Feng, N. N. Mao, J. X. Wu, H. Xu, C. M. Wang, J. Zhang and L. M. Xie, *ACS Nano*, 2015, **9**, 7450–7455.

18 S. Jeong, D. Yoo, M. Ahn, P. Miró, T. Heine and J. Cheon, *Nat. Commun.*, 2015, **6**, 5763.

19 X. L. Li, J. P. Ge and Y. D. Li, *Chem. – Eur. J.*, 2004, **10**, 6163–6171.

20 W. Y. Ge, K. Kawahara, M. Tsuji and H. Ago, *Nanoscale*, 2013, **5**, 5773–5778.

21 L. E. Conroy and K. C. Park, *Inorg. Chem.*, 1968, **7**, 459–463.

22 T. J. Wreting, *J. Phys. Chem. Solids*, 1970, **31**, 2148–2151.

23 S. Tongay, J. Zhou, C. Ataca, K. Lo, T. S. Matthews, J. B. Li, J. C. Grossman and J. Q. Wu, *Nano Lett.*, 2012, **12**, 5576–5580.

24 Z. Wen Xu, H. Zhi Shuo, Z. Wan Li and L. Yan Rong, *Nano Res.*, 2014, **7**, 1731–1737.

25 L. Li, X. S. Fang, T. Y. Zhai, M. Y. Liao, U. K. Gautam, X. C. Wu, Y. Koide, Y. Bando and D. Golberg, *Adv. Mater.*, 2010, **22**, 4151–4156.

26 X. R. Zhang, Z. S. Meng, D. W. Rao, Y. H. Wang, Q. Shi, Y. Z. Liu, H. P. Wu, K. M. Deng, H. Y. Liu and R. F. Lu, *Energy Environ. Sci.*, 2016, **9**, 841–849.

27 Y. L. Zhang, X. C. Wu, Y. R. Tao, C. J. Mao and J. J. Zhu, *Chem. Commun.*, 2008, 2683–2685.

28 M. Zhang, Y. M. Zhu, X. S. Wang, Q. L. Feng, S. L. Qiao, W. Wen, Y. F. Chen, M. H. Cui, J. Zhang, C. Z. Cai and L. M. Xie, *J. Am. Chem. Soc.*, 2015, **137**, 7051–7054.

29 L. Li, H. Q. Wang, X. S. Fang, T. Y. Zhai, Y. Bando and D. Golberg, *Energy Environ. Sci.*, 2011, **4**, 2586–2590.

30 K. H. Zhang, S. M. Feng, J. J. Wang, A. Azcatl, N. Lu, R. Addou, N. Wang, C. Zhou, J. Lerach, V. Bojan, M. J. Kim, L. Q. Chen, R. M. Wallace, M. Terrones, J. Zhu and J. A. Robinson, *Nano Lett.*, 2015, **15**, 6586–6591.

31 L. Lin and Z. F. Liu, *Nat. Mater.*, 2016, **15**, 9–10.

32 Y. Li, J. Kang and J. B. Li, *RSC Adv.*, 2014, **4**, 7396–7401.

33 L. Roubi and C. Carlone, *Phys. Rev. B: Condens. Matter Mater. Phys.*, 1988, **37**, 6808–6812.

34 C. Li, L. Huang, G. P. Snigdha, Y. F. Yu and L. Y. Cao, *ACS Nano*, 2012, **6**, 8868–8877.

35 G. W. Shim, K. Yoo, S. B. Seo, J. Shin, D. Y. Jung, I. S. Kang, C. W. Ahn, B. J. Cho and S. Y. Choi, *ACS Nano*, 2014, **8**, 6655–6662.

36 I. Markov and A. Milchev, *Thin Solid Films*, 1985, **126**, 83–93.

37 D. Mishra, D. Greving, G. A. B. Confalonieri, J. Perlich, B. P. Toperverg, H. Zabel and O. Petracic, *Nanotechnology*, 2014, **25**, 205602.

38 L. Schimka, J. Harl, A. Stroppa, A. Grueneis, M. Marsman, F. Mittendorfer and G. Kresse, *Nat. Mater.*, 2010, **9**, 741–744.

39 S. Y. Liem, G. Kresse and J. H. R. Clarke, *Surf. Sci.*, 1998, **415**, 194–211.

40 R. I. Eglitis and D. Vanderbilt, *Phys. Rev. B: Condens. Matter Mater. Phys.*, 2008, **77**, 195408.

41 J. Hafner, *J. Comput. Chem.*, 2008, **29**, 2044–2078.

42 J. P. Perdew, K. Burke and M. Ernzerhof, *Phys. Rev. Lett.*, 1996, **77**, 3865–3868.

43 A. H. Reshak and S. Auluck, *Physica B*, 2004, **353**, 230–237.

44 D. S. Tsai, K. K. Liu, D. H. Lien, M. L. Tsai, C. F. Kang, C. A. Lin, L. J. Li and J. H. He, *ACS Nano*, 2013, **7**, 3905–3911.

45 P. Hu, Z. Wen, L. Wang, P. Tan and K. Xiao, *ACS Nano*, 2012, **6**, 5988–5994.